Calculation of Hub Loads at Low Airspeeds with Active Control

Sesi Kottapalli
Flight Vehicle Research and Technology Division
NASA Ames Research Center
Moffett Field, California
Sesi.B.Kottapalli@nasa.gov

The effect of individual blade control (IBC) on the full-scale, low airspeed, level flight UH-60A oscillatory fixed system 4P hub loads and the rotating system blade bending moments is studied. The effect of a single 3P IBC input has been considered in this analytical study. At the low speed under consideration, it has been found that convergence of the comprehensive analysis is important for obtaining good predictions. Good correlation has been obtained with the measured full-scale wind tunnel data for the shapes of the fixed system 4P hub loads variations with the 3P IBC input phase, and also for the "best" phase of the 3P input (for minimum hub loads). The blade bending moment comparison shows mixed results. The 3P lead lag and the 4P flap bending moment trends with the 3P IBC input phase are reasonably predicted, whereas the 5P lead lag bending moment trend is not predicted well. Finally, the prediction of the baseline (no IBC) bending moments needs further study.

Notation

C_T	Rotor thrust coefficient
IBC	Individual Blade Control
LRTA	Large Rotor Test Apparatus, NASA Ames
N	Number of main rotor blades, N = 4 for the UH-60A
NP	Integer (N) multiple of main rotor speed
P	Per revolution
u_{IBC}	IBC control input, $\sum_{n=2}^{7} -A_n \cos(n\psi_1 - \phi_n)$, for blade no. 1 (i.e., blade no. 4 in CAMRAD II), deg
μ	Rotor advance ratio
σ	Rotor solidity ratio
ϕ_n	Phase of n'th harmonic of u_{IBC}

Introduction

At present, the low airspeed vibration of helicopters cannot be predicted with confidence. The introduction of active control increases the complexity of the prediction problem. Accurate and reliable "first-principles" based predictions of the helicopter fuselage vibration with active control are not yet available.

The present initial study considers the first step in the prediction of the helicopter fuselage vibration. In this study, a fixed, rigid hub is considered, i.e., the fuselage effects are not included. The effect of individual blade control (IBC) on the full-scale, low airspeed, level flight UH-60A vibratory NP hub loads is under consideration. The rotorcraft comprehensive analysis CAMRAD II (Refs. 1-3) is used. The basic CAMRAD/UH-60A master input database files (without IBC modeling) were obtained from H. Yeo (Refs. 4-5).

The calculations from this study are compared with the measured low airspeed full-scale UH-60A rotor-only wind tunnel database (Refs. 6-8) that was acquired in the NASA Ames 80- by 120-Foot Wind Tunnel with the Large Rotor Test Apparatus (LRTA). The IBC related wind tunnel testing was described in Ref. 6. The measurements included the oscillatory hub loads obtained from a five-component rotor balance to measure the rotor hub loads (Ref. 7).

The objective of this paper is to present comparisons of the measured and predicted oscillatory fixed system 4P hub forces at low speeds with active control. The focus is on the qualitative comparison of the hub loads, i.e., the basic shapes of the oscillatory fixed system 4P hub loads variations with the phase of a single IBC input are being compared. The "best" phase for minimum hub loads is also being compared. In order to understand the sources of the reductions in the hub loads due to IBC at low speed under consideration, this paper also includes comparisons of the measured and predicted 3P and 5P lead lag bending moments and the 4P flap bending moments.

Presented at the American Helicopter Society 63rd Annual Forum, Virginia Beach, VA, May 1-3, 2007.

Measured Wind Tunnel Hub Loads

Figures 1 to 3 show the measured (Ref. 6, $\mu = 0.107$ and $C_T/\sigma = 0.0733$) fixed system 4P axial, side, and normal hub force variations with the phase of the 3P IBC input, respectively. Figure 1 shows that the measured 4P axial force has a minimum value between 270 deg and 315 deg. Figure 2 shows that the measured 4P side force has a minimum value in the neighborhood of 315 deg. Figure 3 shows that the measured 4P normal force has a minimum value between 225 deg and 270 deg.

The above 4P experimental hub loads are discussed as follows. A shake test of the LRTA was conducted, and Ref. 7 discusses the present rotor balance characteristics in the following manner: "During the shake test, data were also acquired to evaluate the dynamic characteristics of the rotor balance. Although these data were not sufficient for a complete dynamic calibration of the balance…, they did provide an indication of balance characteristics." Table 1 gives the amplification factors that were obtained from the above shake test (i.e., static calibration). The amplification factors (magnitude ratios) for the above fixed system, in-plane hub forces at 4P are not close to 1. A comparison of the actual magnitudes of the measured and predicted fixed system 4P hub loads is not possible in the absence of the availability of a dynamic calibration matrix (that includes cross coupling terms and their effect also on the above phase). Thus, in the absence of a complete dynamic calibration of the LRTA rotor balance, any analytical effort that attempts to predict the oscillatory fixed system 4P hub loads with IBC must necessarily compare only the relevant waveform *shape* and the "best" IBC *phase* value for minimum fixed system 4P hub loads. The actual magnitudes of the measured and the predicted fixed system 4P hub loads are not being compared in this study. The relevant waveform shapes and the "best" phase values for minimum hub loads are under consideration.

Results

The results in this paper are given for the following operating condition: $\mu = 0.107$ and $C_T/\sigma = 0.0733$. The free wake model in CAMRAD II has been used (multiple trailer wake model with consolidation, compression form).

A single 3P IBC input (0.5 deg amplitude) has been used and the 3P input phase has been varied from 0 deg to 315 deg in 45 deg increments. At the low speed under consideration, it has been found that convergence is important for obtaining good predictions, discussed as follows.

Hub Loads Convergence Study

Within the comprehensive analysis, convergence of the trim and circulation loops is critically important in the present low speed application (advance ratio = 0.107, with active control) in which the free wake plays a very important role in the prediction of the oscillatory blade loads (and the fixed system 4P hub loads). In this study, the effects of the changes in the trim and the circulation tolerances and the number of free wake iterations on the fixed system 4P hub loads have been systematically studied. The predicted results that are discussed below have been obtained subsequent to a successfully completed convergence study. The following sections contain the corresponding Basic Variations (the control angles, etc.), the Hub Loads Comparison, and the Blade Bending Moments Comparison.

Basic Variations

Figures 4a-4b show the measured and predicted variations of the cosine and sine components of the 3P IBC input. The measured 3P IBC inputs shown in Figs. 4a-4b are based on the IBC actuator position obtained from LVDT measurements. For the predicted variations, both the 3P input actuator commands and the resulting 3P pitch joint variations are shown in Figs. 4a-4b. The differences between the measured IBC inputs, the predicted actuator commands, and the predicted pitch joint variations are due to the control system flexibility, i.e., the spring at the pitch joint, and the pitch joint measurement system flexibility. The control angles (the collective and the cyclics) required to trim the rotor are shown in Fig. 5. Table 2 shows the CAMRAD II blade frequencies.

In addition, the variations of the parameters that are not "trim variables" are shown in Figs. 6 to 8, as follows: the rotor drag (Fig. 6), the rotor power (total and induced, Fig. 7), and the ratio of the induced power to the minimum induced power (Fig. 8).

Hub Loads Comparison

Figures 9 to 11 show the measured and the CAMRAD II predicted, fixed system 4P axial, side, and normal hub force variations with the phase of the 3P IBC input, respectively. In Figs. 9a, 10a, and 11a the actual CAMRAD II predicted 4P hub loads are shown. In Figs. 9b, 10b, and 11b, the measured and predicted 4P hub loads have been scaled to their respective maximum values in order to facilitate the comparison of the measured and predicted data. As discussed earlier, the absolute magnitudes of the measured and predicted 4P hub forces are not being compared. The relevant

waveform shapes and the "best" phase values for minimum hub loads are under consideration. Overall, Figs. 9b, 10b, and 11b show that the respective measured and predicted waveform shapes compare reasonably well. Specific comparisons for the "best" phase for minimum hub loads are given as follows. Figure 9b shows that both the measured and the predicted 4P axial forces have minimum values in the neighborhood of 270 deg to 315 deg. Figure 10b shows that both the measured and the predicted 4P side forces have minimum values in the neighborhood of 315 deg. Figure 11b shows that both the measured and the predicted 4P normal forces have minimum values in the neighborhood of 270 deg.

Blade Bending Moments Comparison

This group of results includes the measured and the predicted oscillatory blade bending moments (the 3P and 5P in-plane (lead lag) bending moments and the 4P out-of-plane (flap) bending moment). Since the actual magnitudes of the measured and the predicted fixed system 4P hub loads are not being compared in this study, a comparison of the corresponding oscillatory blade bending moments should help understand the sources of the reductions in the fixed system 4P hub loads. In the following comparisons, blade bending moment variations with the phase of the single 3P IBC input are shown at the following three radial stations: 0.20R, 0.50R, and 0.70R.

3P Lead lag Bending Moments. Figures 12 to 14 show the measured and predicted 3P lead lag bending moment variations at the selected three radial stations. Figures 12 to 14 show that the trends in the 3P lead lag bending moment due to the single 3P IBC input are captured well by the analysis. Also, the optimum 3P IBC input phase (in the neighborhood of 270 to 315 deg) uniformly reduces both the measured and predicted 3P lead lag bending moment at all three radial stations. The baseline 3P lead lag bending moment is predicted well only at the mid span location. Both test and analysis, Figs. 12 to 14, indicate that the reductions in the fixed system 4P in-plane forces (axial and side forces) may be due to the reductions in the 3P lead lag bending moment, i.e., the 3P lead lag (in-plane) response.

5P Lead lag Bending Moments. Figures 15 to 17 show the measured and predicted 5P lead lag bending moment variations at the selected three radial stations. The measured and predicted 5P lead lag bending moment variations (baseline and with IBC) show different trends, Figs. 15 to 17. To understand the reason for this discrepancy, the measured and predicted lead lag bending moment time histories for the following two conditions have been studied: the baseline, no IBC, condition and the "best" 3P IBC input phase (270 deg) condition. The above time histories for the above three radial stations are discussed as follows in Figs. 18 to 29.

Figures 18 to 23 show the measured and predicted time histories with their respective mean values removed. The baseline, no IBC, measured and predicted lead lag bending moment time histories are shown in Figs. 18 to 20. The above baseline time histories, Figs. 18 to 20, are in reasonable agreement except at the inboard section, 0.20R. Figures 21 to 23 show the corresponding time histories for the 270 deg 3P IBC input condition. Comparison of the measured and predicted "with IBC" time histories, Figs. 21 to 23, shows a lack of agreement for the phase, even though the changes due to IBC at the 270 deg *azimuthal* location (retreating blade) are being picked up somewhat by the analysis (Figs. 18 and 21, 19 and 22, and 20 and 23).

Figures 24 to 29 show the measured and predicted time histories constructed using only the 3P, 4P, and 5P harmonic components (called the "3P-5P time histories"). The baseline, no IBC, measured and predicted lead lag bending moment 3P-5P time histories are shown in Figs. 24 to 26. The above baseline 3P-5P time histories, Figs. 24 to 26, are in reasonable agreement, though the predicted amplitudes are smaller that the measured amplitudes. Figures 27 to 29 show the corresponding 3P-5P time histories for the 270 deg 3P IBC input condition. The increase in the 5P harmonic component, from its baseline value, due to the 270 deg 3P IBC input is evident in both the test and analytical 3P-5P time histories (Figs. 15, 24, 27, and 16, 25, 28, and 17, 26, 29). The "with IBC" 3P-5P time histories, Figs. 27 to 29, show a lack of agreement for the phase. Overall, it is clear from the above comparison of the measured and predicted lead lag bending moment time histories that further analysis is required to capture the details of the measured effects of IBC on the higher harmonic components of the lead lag bending moments.

4P Flap Bending Moments. Figures 30 to 32 show the measured and predicted 4P flap bending moment variations at the selected three radial stations. Figures 30 to 32 show that the measured trends in the 4P flap moment due to the single 3P IBC input are fairly well predicted by the analysis. The predicted baseline 4P flap bending moments are not captured well.

Conclusions

The prediction of the oscillatory fixed system 4P hub loads (and the rotating system 3P, 4P, and 5P blade bending moments) at low airspeeds with a single 3P IBC input has been considered in this analytical study. Specific conclusions are as follows:

1. Good correlation has been obtained with measured full-scale wind tunnel data for the shapes of the fixed system 4P hub loads variations with the 3P IBC input phase, and also for the "best" phase of the 3P input (for minimum hub loads).
2. The blade bending comparisons show mixed results. The trends of the 3P lead lag and the 4P flap bending moments due to the single 3P IBC input phase are reasonably predicted by the analysis. However, the 5P lead lag bending moment variation is not predicted well by the analysis. In general, the prediction of the baseline, no IBC, blade bending moments needs further study.

References

1. Johnson, W. "CAMRAD II, Comprehensive Analytical Model of Rotorcraft Aerodynamics and Dynamics," Johnson Aeronautics, Palo Alto, California, 1992-1999.

2. Johnson, W. "Technology Drivers in the Development of CAMRAD II," American Helicopter Society, American Helicopter Society Aeromechanics Specialists Conference, San Francisco, CA, January 19-21, 1994.

3. Johnson, W. "A General Free Wake Geometry Calculation for Wings and Rotors," American Helicopter Society 51st Annual Forum Proceedings, Ft. Worth, TX, May 9-11, 1995.

4. Yeo, H. and Johnson, W., "Assessment of Comprehensive Analysis Calculation of Airloads on Helicopter Rotors," *AIAA Journal of Aircraft*, Vol. 42, No. 5, September-October 2005, pp. 1218-1228.

5. Yeo, H. and Johnson, W., "Assessment of Comprehensive Analysis Calculation of Structural Loads on Rotors," American Helicopter Society 60th Annual Forum Proceedings, Baltimore, Maryland, June 7-10, 2004.

6. Jacklin, S. A., Haber, A., de Simone, G., Norman, T. R., Kitaplioglu, C., and Shinoda, P. M., "Full-Scale Wind Tunnel Test of an Individual Blade Control System for a UH-60 Helicopter," American Helicopter Society 58th Annual Forum Proceedings, Montreal, Canada, June 11-13, 2002.

7. Norman, T. R., Shinoda, P. M., Jacklin, S. A., and Sheikman, A., "Low-Speed Wind Tunnel Investigation of a Full-Scale UH-60 Rotor System," American Helicopter Society 58th Annual Forum Proceedings, Montreal, Canada, June 11-13, 2002.

8. Shinoda, P., Yeo, H., and Norman, T.R., "Rotor Performance of a UH-60 Rotor System in the NASA Ames 80- by 120-Foot Wind Tunnel," *Journal of the American Helicopter Society*, Vol. 49, No. 4, October 2004, pp. 401-413.

Table 1. Frequency Response of LRTA Balance in Side and Axial Directions (Ref. 7, single axis loading applied at the hub)

Direction	Frequency	Magnitude Ratio	Phase, deg
Side Force	1P	0.90	0
	4P	2.85	-30
Axial Force	1P	0.93	-3
	4P	1.87	-8

Table 2. Predicted (CAMRAD II) UH-60A Blade Frequencies at 100%NR

Blade Mode	Frequency (Per Rev)
Lead lag 1	0.27
Flap 1	1.03
Flap 2	2.82
Torsion 1	4.50
Lead lag 2	4.62
Flap 3	5.31

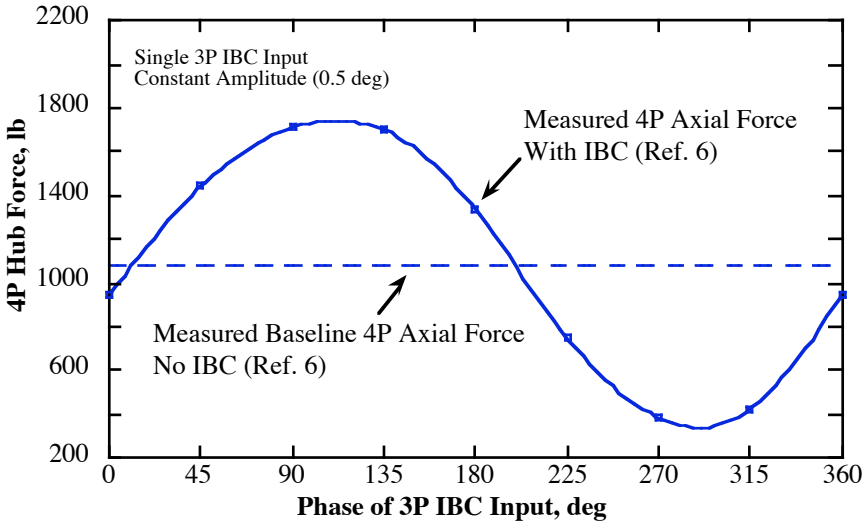

Fig. 1. Measured wind tunnel UH-60A 4P axial force variation with 3P IBC input phase, $\mu = 0.107$, $C_T/\sigma = 0.0733$ (Ref. 6).

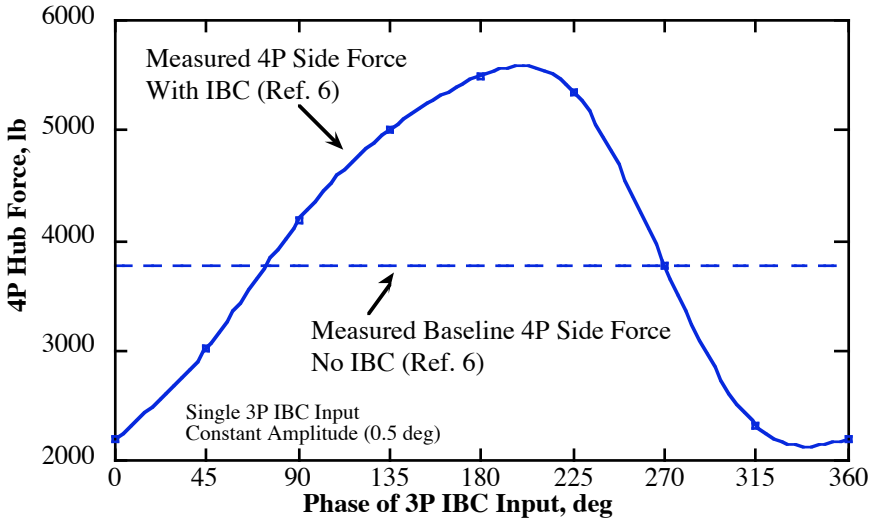

Fig. 2. **Measured wind tunnel UH-60A 4P side force variation with 3P IBC input phase, $\mu = 0.107$, $C_T/\sigma = 0.0733$ (Ref. 6).**

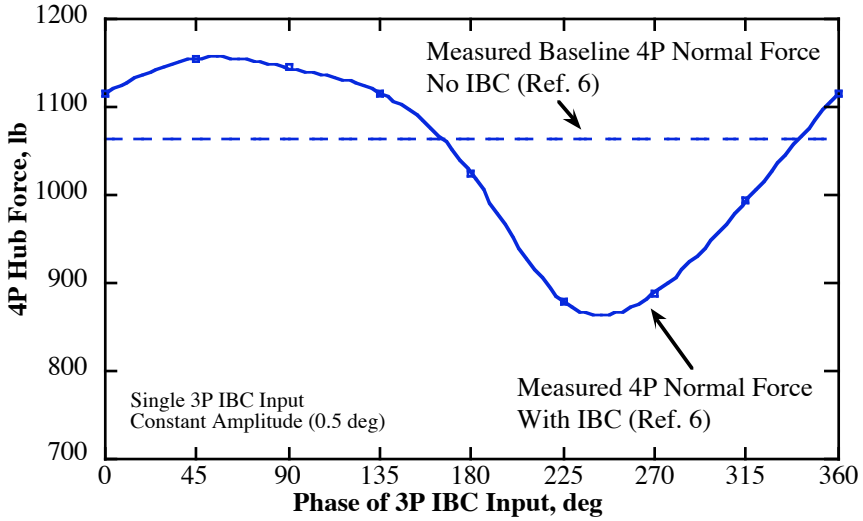

Fig. 3. **Measured wind tunnel UH-60A 4P normal force variation with 3P IBC input phase, $\mu = 0.107$, $C_T/\sigma = 0.0733$ (Ref. 6).**

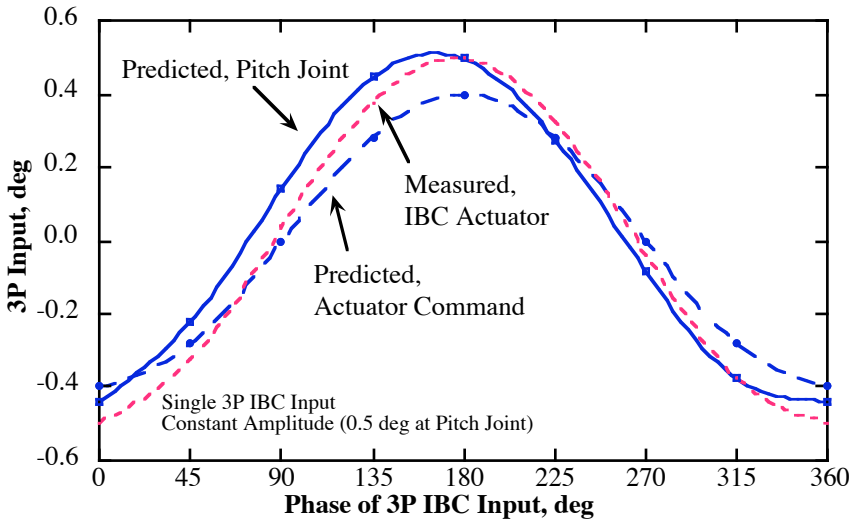

Fig. 4a. Measured and predicted (CAMRAD II) cosine components of 3P IBC pitch input, $\mu = 0.107$, $C_T/\sigma = 0.0733$.

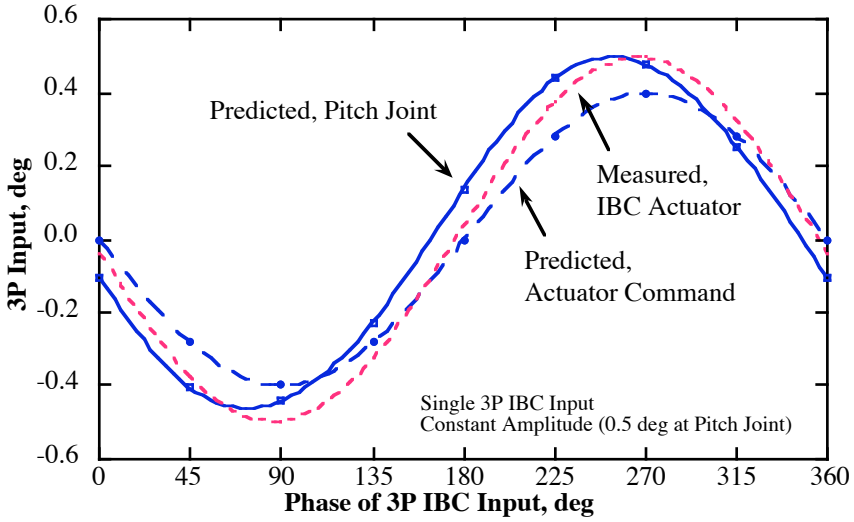

Fig. 4b. Measured and predicted (CAMRAD II) sine components of 3P IBC pitch input, $\mu = 0.107$, $C_T/\sigma = 0.0733$.

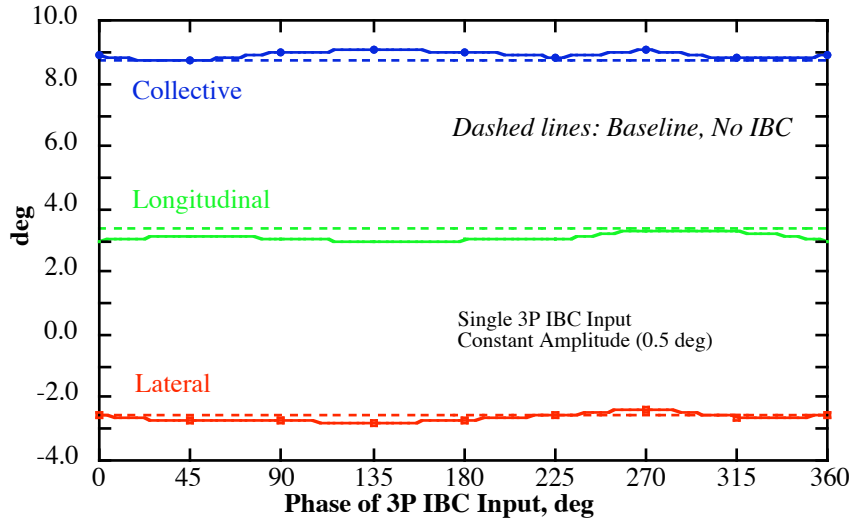

Fig. 5. Predicted (CAMRAD II) control angles required for trim, $\mu = 0.107$, $C_T/\sigma = 0.0733$.

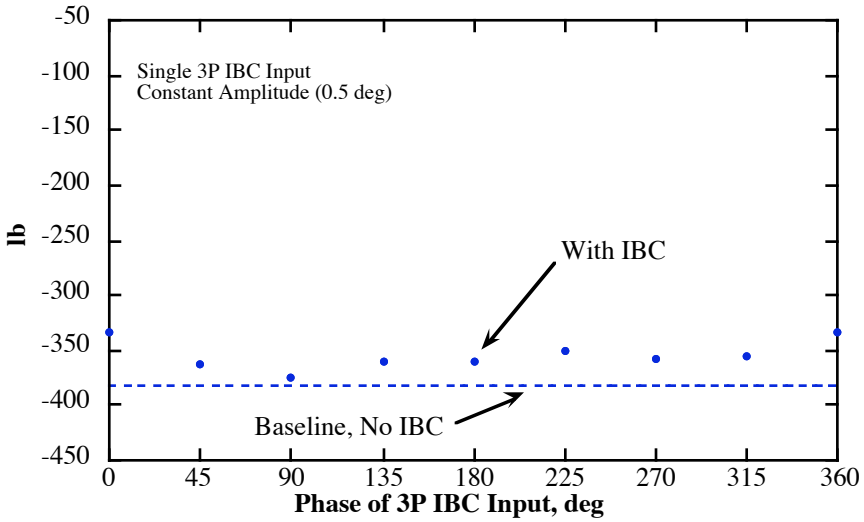

Fig. 6. Predicted (CAMRAD II) drag force, untrimmed, $\mu = 0.107$, $C_T/\sigma = 0.0733$.

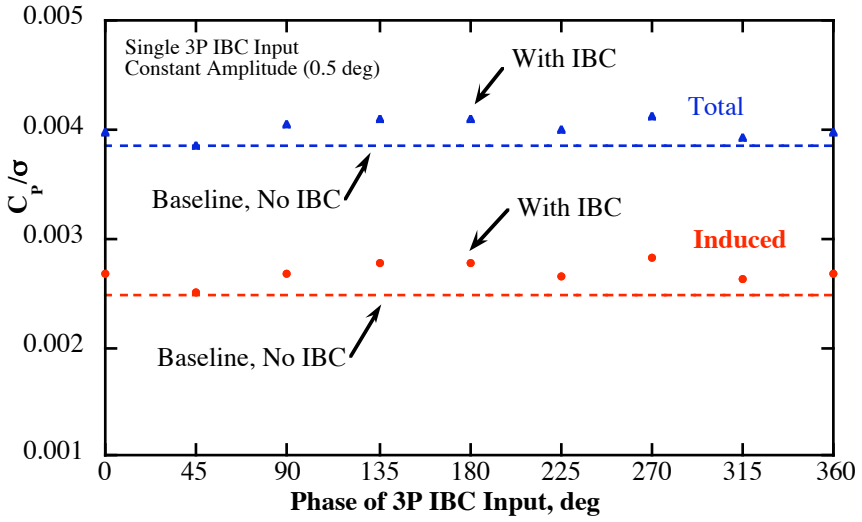

Fig. 7. Predicted (CAMRAD II) power coefficient, untrimmed, $\mu = 0.107$, $C_T/\sigma = 0.0733$.

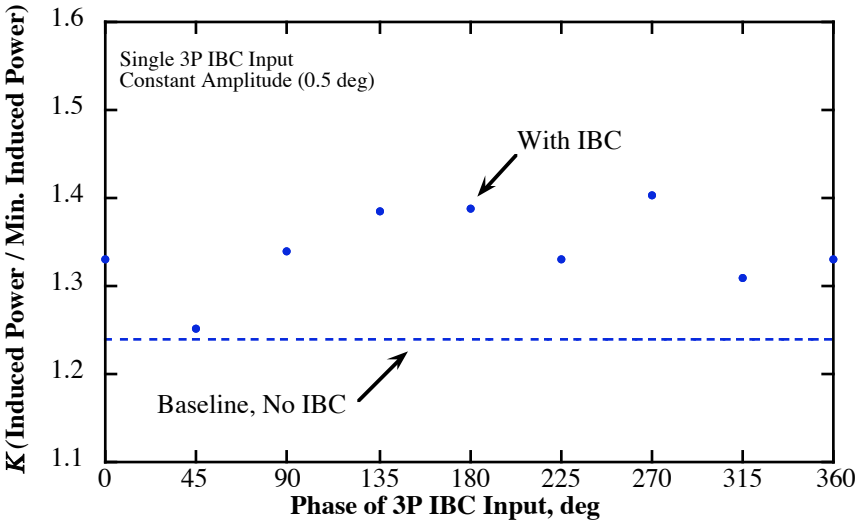

Fig. 8. Predicted (CAMRAD II) ratio of induced power to minimum induced power, untrimmed, $\mu = 0.107$, $C_T/\sigma = 0.0733$.

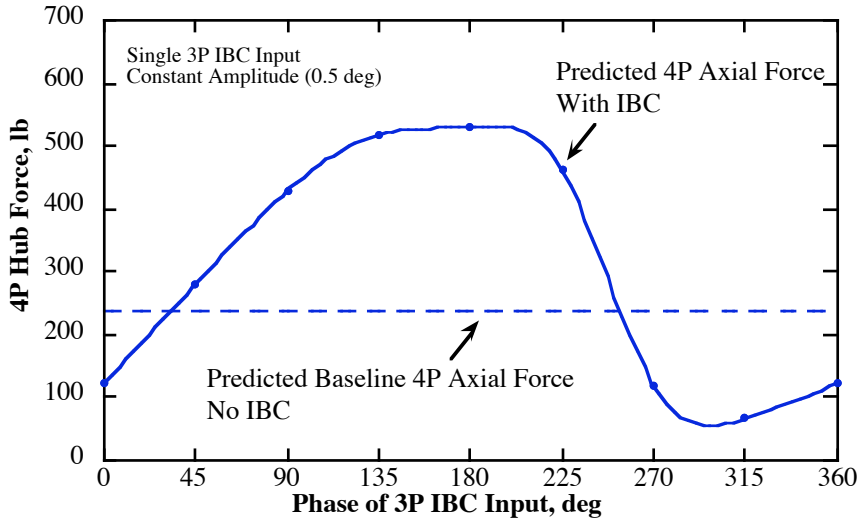

Fig. 9a. Predicted (CAMRAD II) UH-60A 4P axial force variation with 3P IBC input phase, $\mu = 0.107$, $C_T/\sigma = 0.0733$.

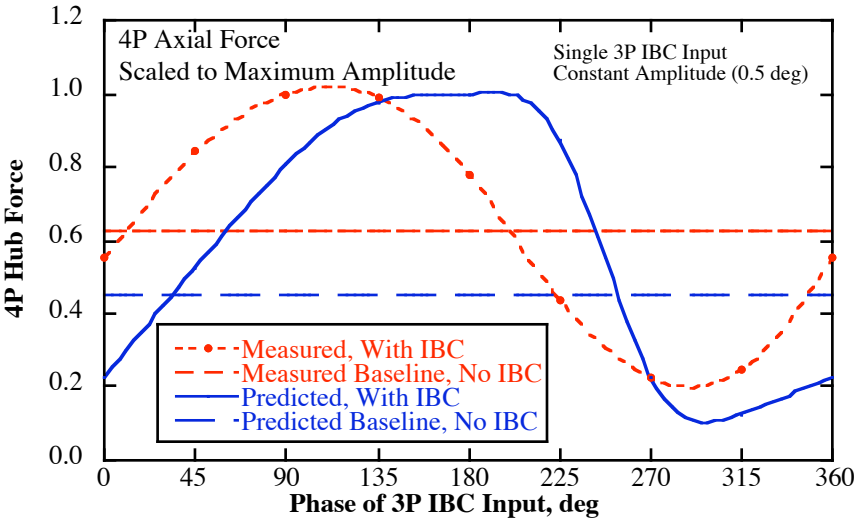

Fig. 9b. Measured and predicted (CAMRAD II) UH-60A 4P axial force variations with 3P IBC input phase, $\mu = 0.107$, $C_T/\sigma = 0.0733$.

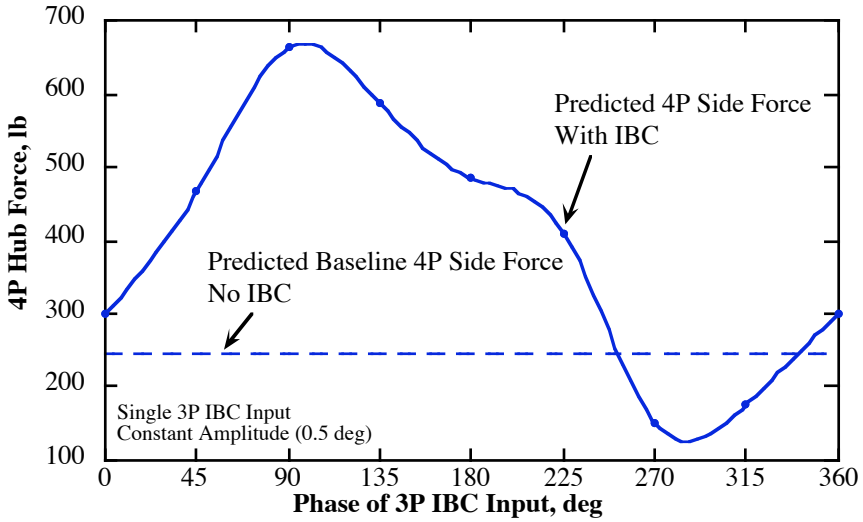

Fig. 10a. Predicted (CAMRAD II) UH-60A 4P side force variation with 3P IBC input phase, $\mu = 0.107$, $C_T/\sigma = 0.0733$.

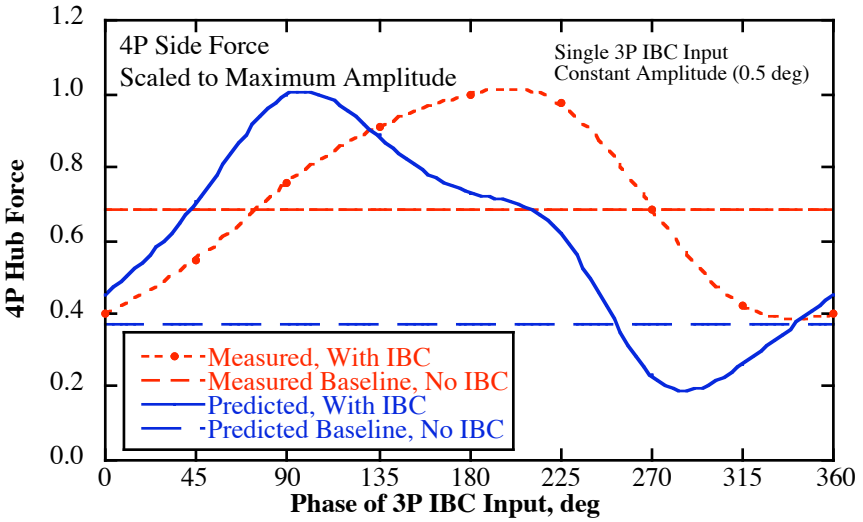

Fig. 10b. Measured and predicted (CAMRAD II) UH-60A 4P side force variations with 3P IBC input phase, $\mu = 0.107$, $C_T/\sigma = 0.0733$.

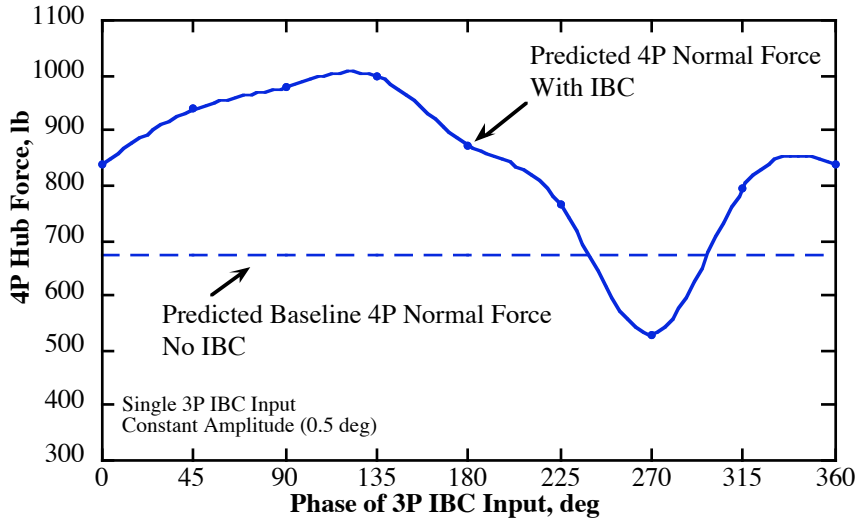

Fig. 11a. Predicted (CAMRAD II) UH-60A 4P normal force variation with 3P IBC input phase, $\mu = 0.107$, $C_T/\sigma = 0.0733$.

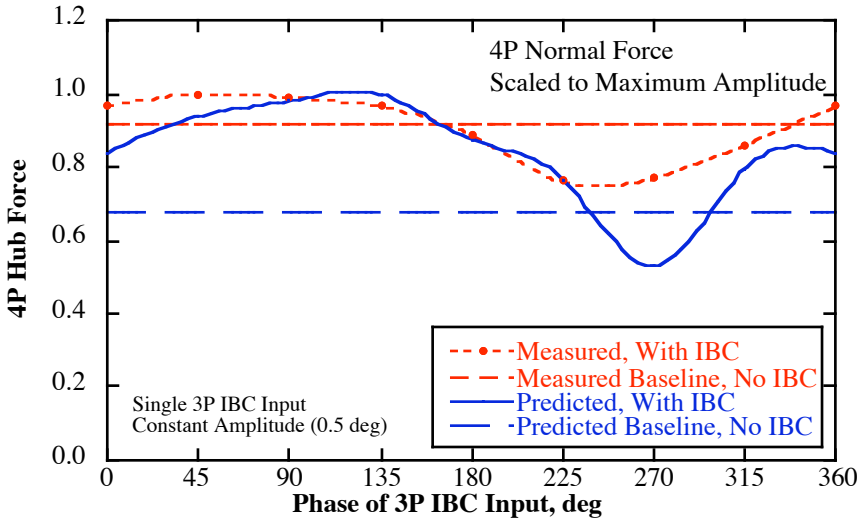

Fig. 11b. Measured and predicted (CAMRAD II) UH-60A 4P normal force variations with 3P IBC input phase, $\mu = 0.107$, $C_T/\sigma = 0.0733$.

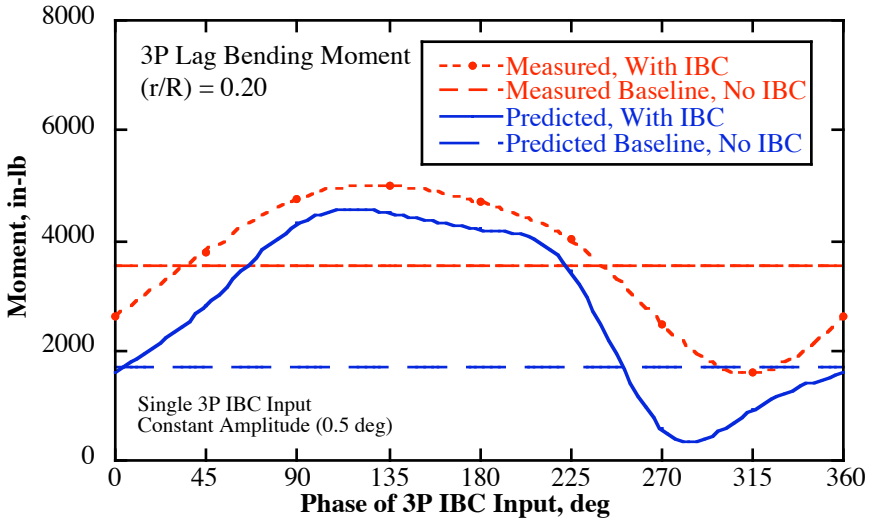

Fig. 12. Measured and predicted (CAMRAD II) UH-60A 3P lag bending moment variations with 3P IBC input phase, (r/R) = 0.20, $\mu = 0.107$, $C_T/\sigma = 0.0733$.

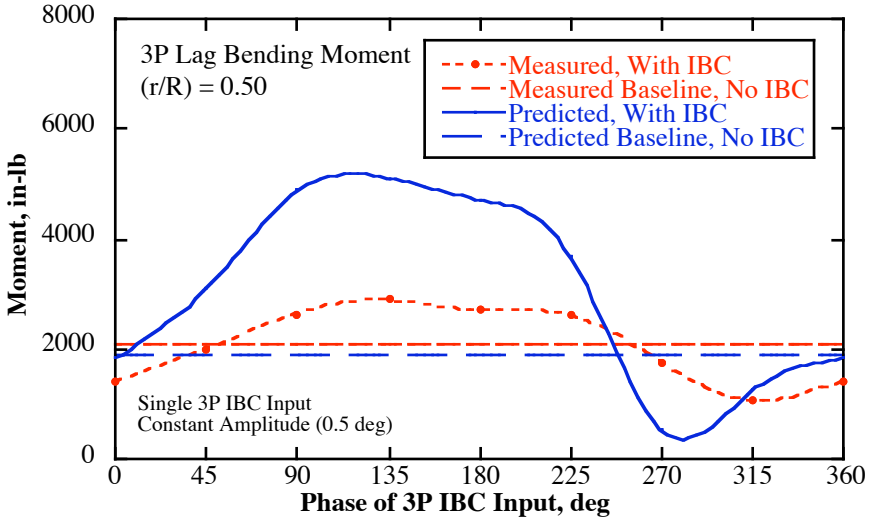

Fig. 13. Measured and predicted (CAMRAD II) UH-60A 3P lag bending moment variations with 3P IBC input phase, (r/R) = 0.50, $\mu = 0.107$, $C_T/\sigma = 0.0733$.

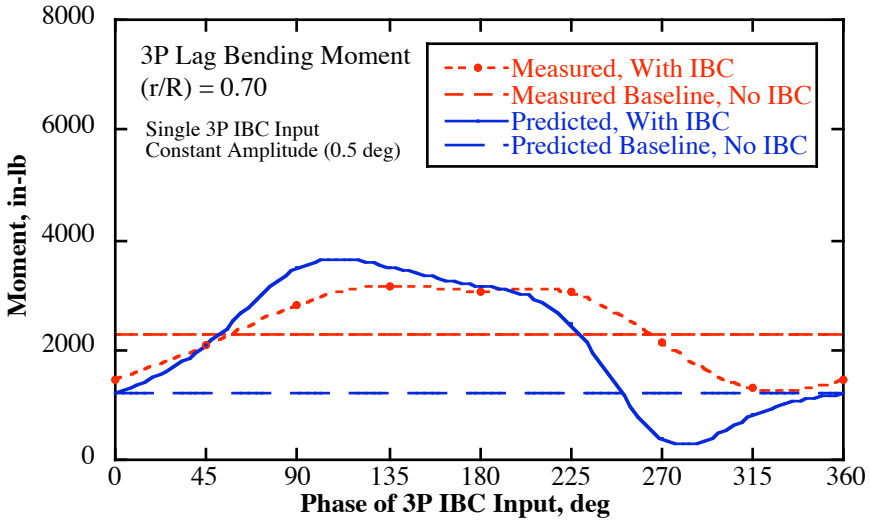

Fig. 14. Measured and predicted (CAMRAD II) UH-60A 3P lag bending moment variations with 3P IBC input phase, (r/R) = 0.70, $\mu = 0.107$, $C_T/\sigma = 0.0733$.

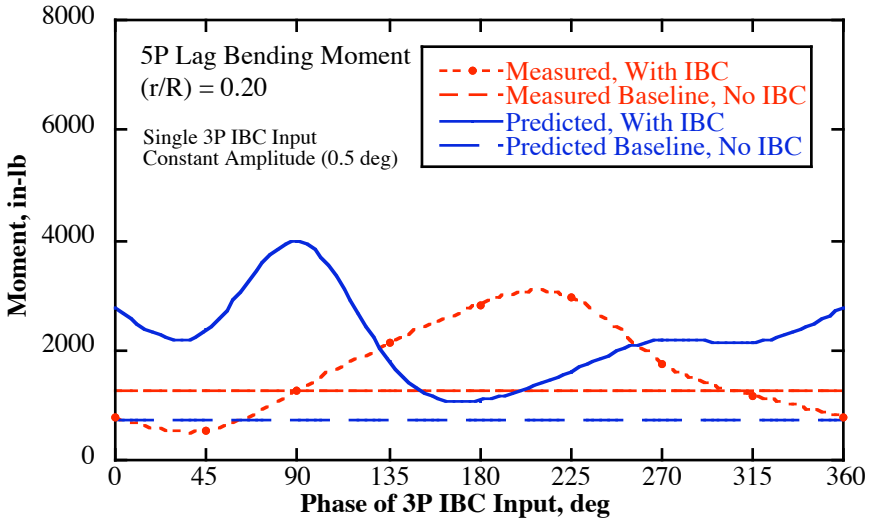

Fig. 15. Measured and predicted (CAMRAD II) UH-60A 5P lag bending moment variations with 3P IBC input phase, (r/R) = 0.20, $\mu = 0.107$, $C_T/\sigma = 0.0733$.

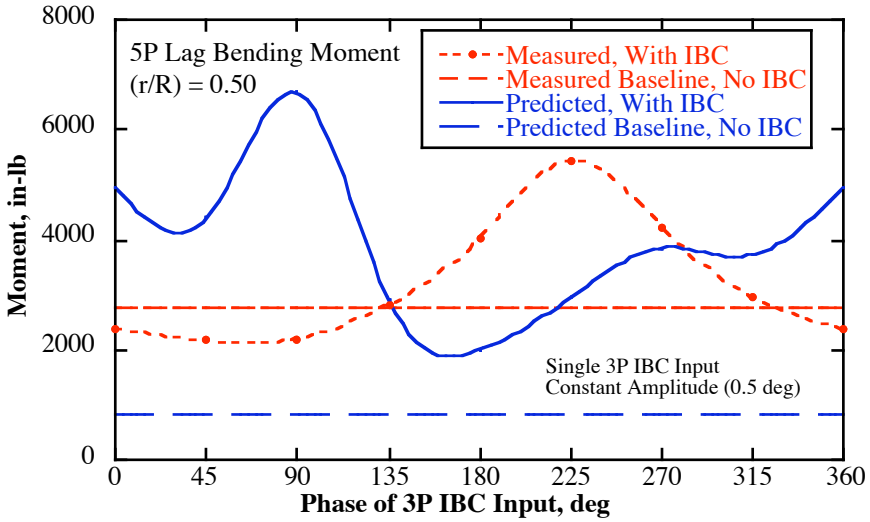

Fig. 16. Measured and predicted (CAMRAD II) UH-60A 5P lag bending moment variations with 3P IBC input phase, (r/R) = 0.50, $\mu = 0.107$, $C_T/\sigma = 0.0733$.

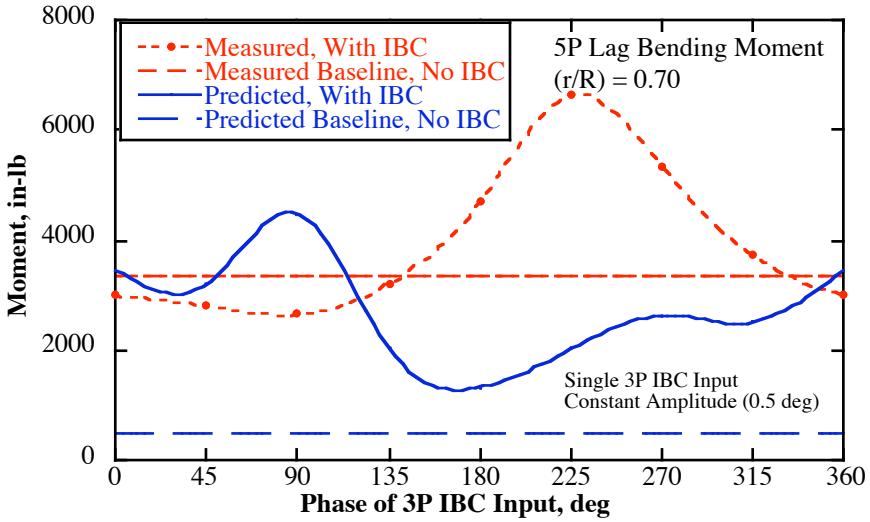

Fig. 17. Measured and predicted (CAMRAD II) UH-60A 5P lag bending moment variations with 3P IBC input phase, (r/R) = 0.70, $\mu = 0.107$, $C_T/\sigma = 0.0733$.

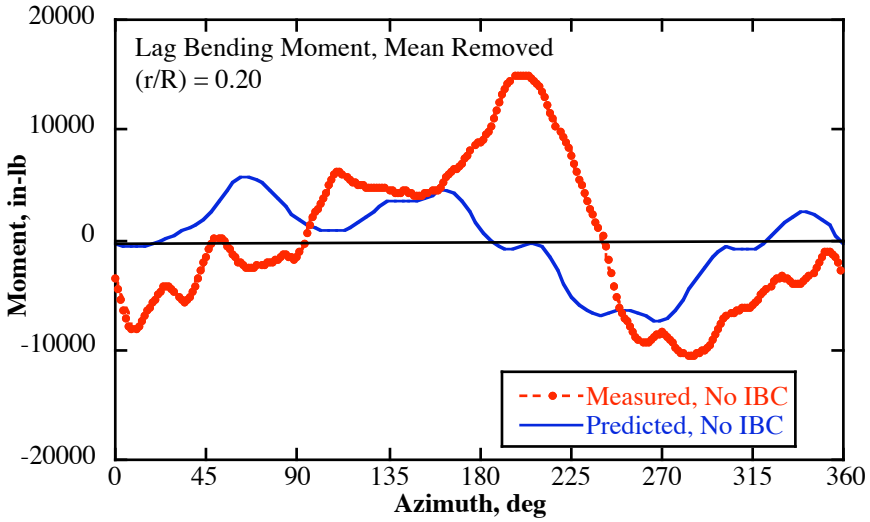

Fig. 18. Baseline measured and predicted (CAMRAD II) UH-60A lag bending moment time histories, (r/R) = 0.20, $\mu = 0.107$, $C_T/\sigma = 0.0733$.

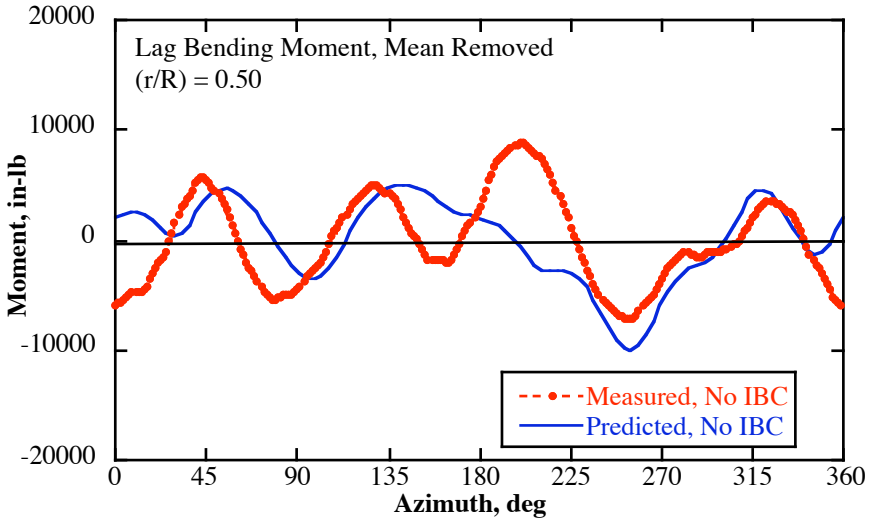

Fig. 19. Baseline measured and predicted (CAMRAD II) UH-60A lag bending moment time histories, (r/R) = 0.50, $\mu = 0.107$, $C_T/\sigma = 0.0733$.

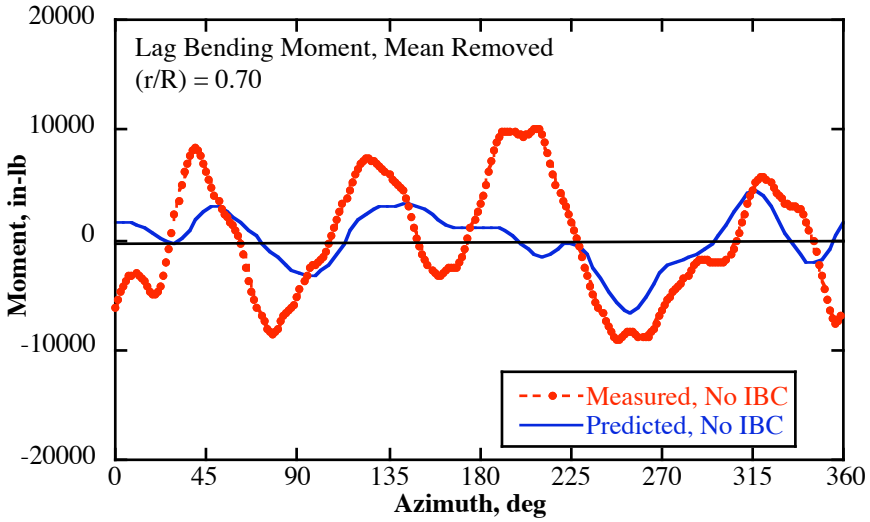

Fig. 20. Baseline measured and predicted (CAMRAD II) UH-60A lag bending moment time histories, (r/R) = 0.70, $\mu = 0.107$, $C_T/\sigma = 0.0733$.

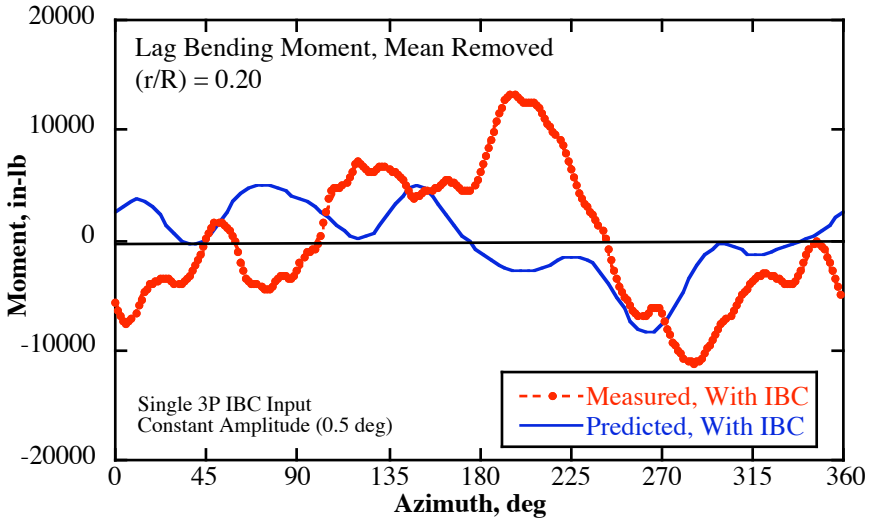

Fig. 21. Best phase (3P IBC input phase = 270 deg) measured and predicted (CAMRAD II) UH-60A lag bending moment time histories, (r/R) = 0.20, $\mu = 0.107$, $C_T/\sigma = 0.0733$.

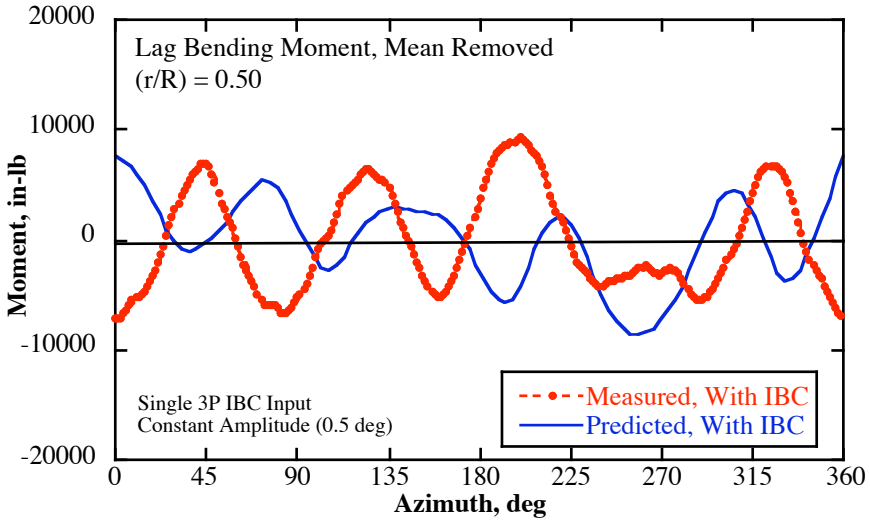

Fig. 22. Best phase (3P IBC input phase = 270 deg) measured and predicted (CAMRAD II) UH-60A lag bending moment time histories, (r/R) = 0.50, μ = 0.107, C_T/σ = 0.0733.

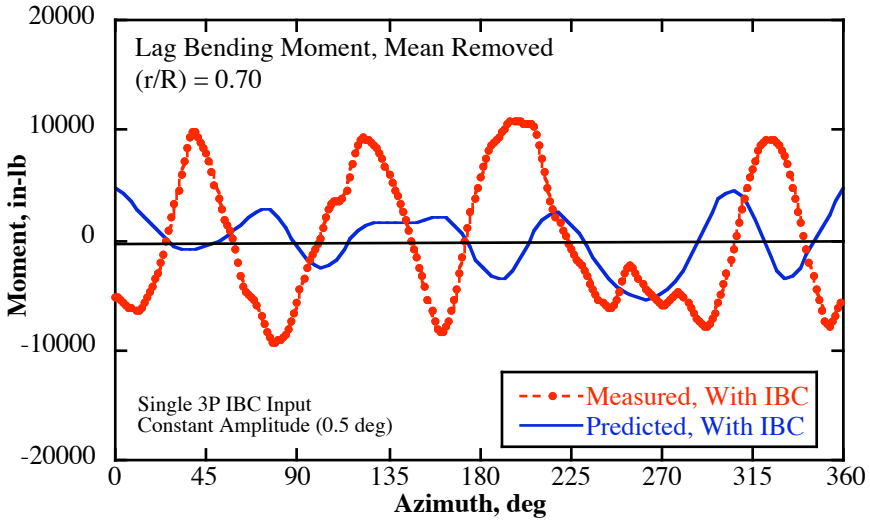

Fig. 23. Best phase (3P IBC input phase = 270 deg) measured and predicted (CAMRAD II) UH-60A lag bending moment time histories, (r/R) = 0.70, μ = 0.107, C_T/σ = 0.0733.

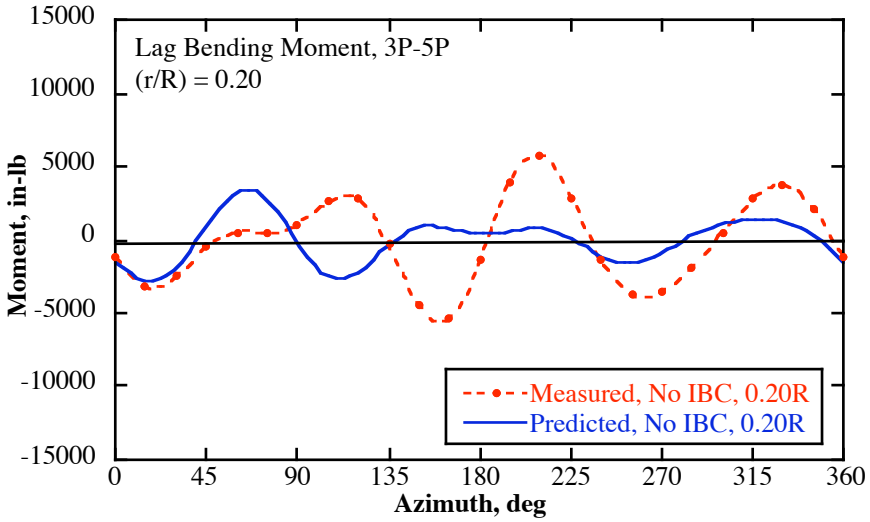

Fig. 24. Baseline measured and predicted (CAMRAD II) UH-60A 3P-5P lag bending moment time histories, (r/R) = 0.20, μ = 0.107, C_T/σ = 0.0733.

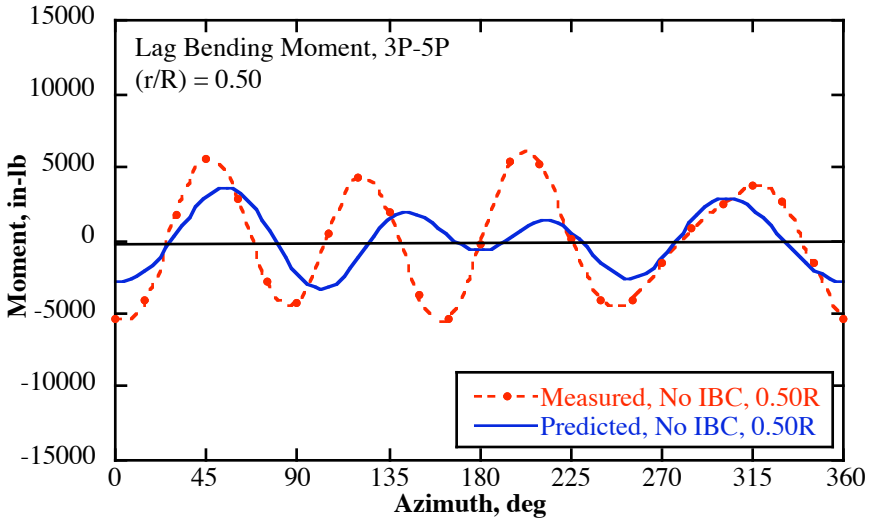

Fig. 25. Baseline measured and predicted (CAMRAD II) UH-60A 3P-5P lag bending moment time histories, (r/R) = 0.50, μ = 0.107, C_T/σ = 0.0733.

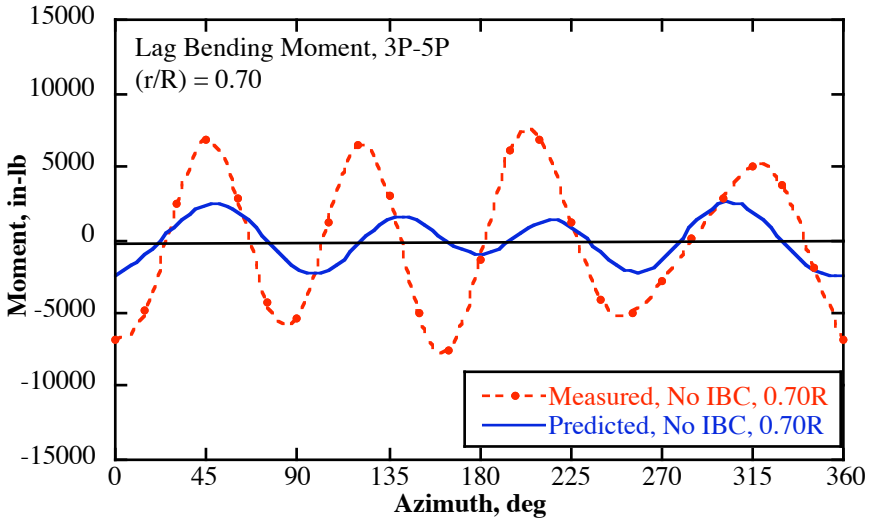

Fig. 26. Baseline measured and predicted (CAMRAD II) UH-60A 3P-5P lag bending moment time histories, (r/R) = 0.70, $\mu = 0.107$, $C_T/\sigma = 0.0733$.

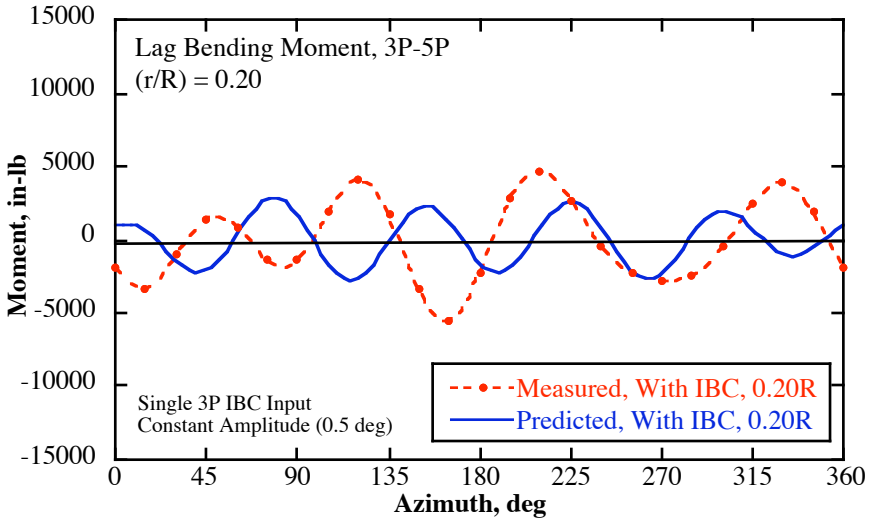

Fig. 27. Best phase (3P IBC input phase = 270 deg) measured and predicted (CAMRAD II) UH-60A 3P-5P lag bending moment time histories, (r/R) = 0.20, $\mu = 0.107$, $C_T/\sigma = 0.0733$

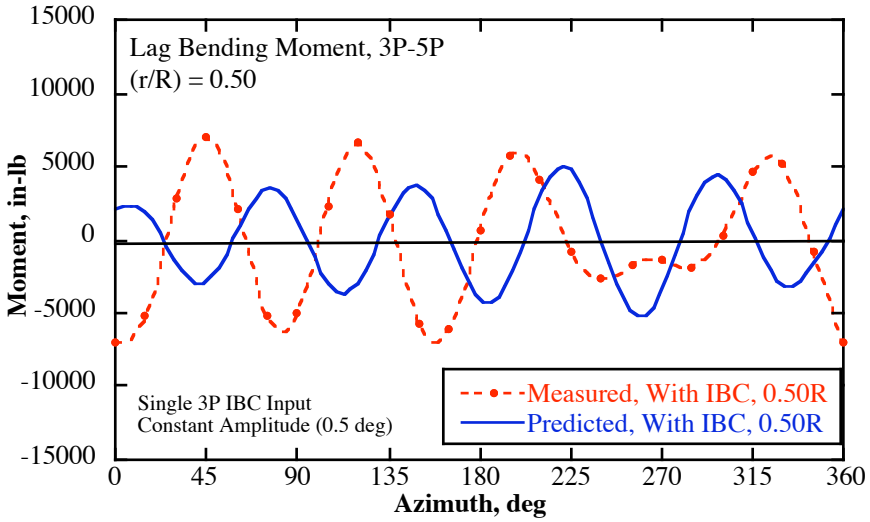

Fig. 28. Best phase (3P IBC input phase = 270 deg) measured and predicted (CAMRAD II) UH-60A 3P-5P lag bending moment time histories, (r/R) = 0.50, μ = 0.107, C_T/σ = 0.0733

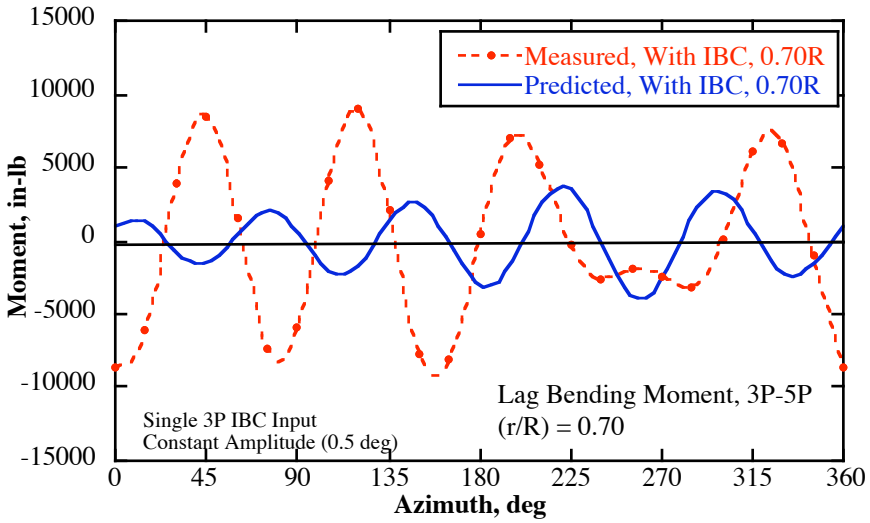

Fig. 29. Best phase (3P IBC input phase = 270 deg) measured and predicted (CAMRAD II) UH-60A 3P-5P lag bending moment time histories, (r/R) = 0.70, μ = 0.107, C_T/σ = 0.0733

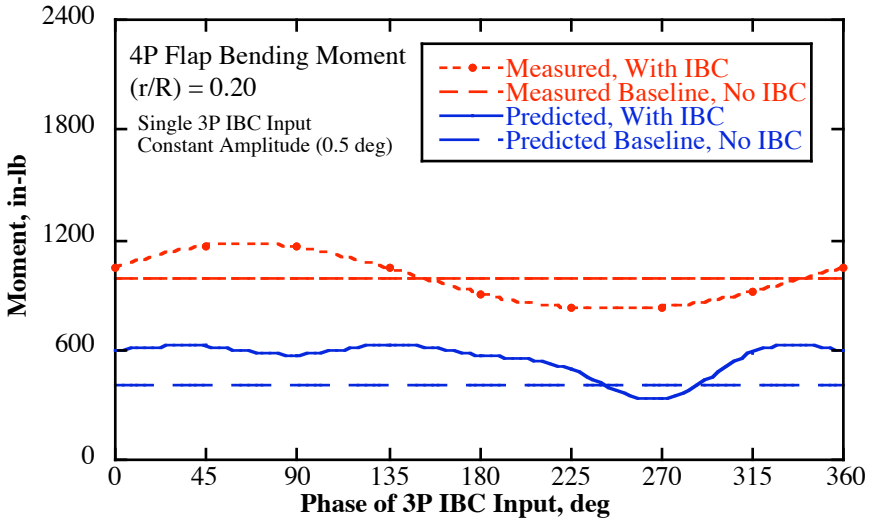

Fig. 30. Measured and predicted (CAMRAD II) UH-60A 4P flap bending moment variations with 3P IBC input phase, (r/R) = 0.20, $\mu = 0.107$, $C_T/\sigma = 0.0733$.

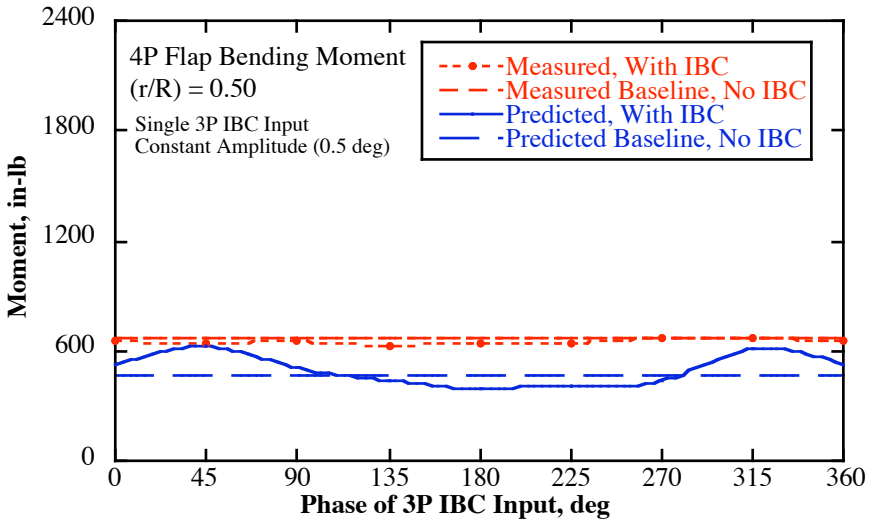

Fig. 31. Measured and predicted (CAMRAD II) UH-60A 4P flap bending moment variations with 3P IBC input phase, (r/R) = 0.50, $\mu = 0.107$, $C_T/\sigma = 0.0733$.

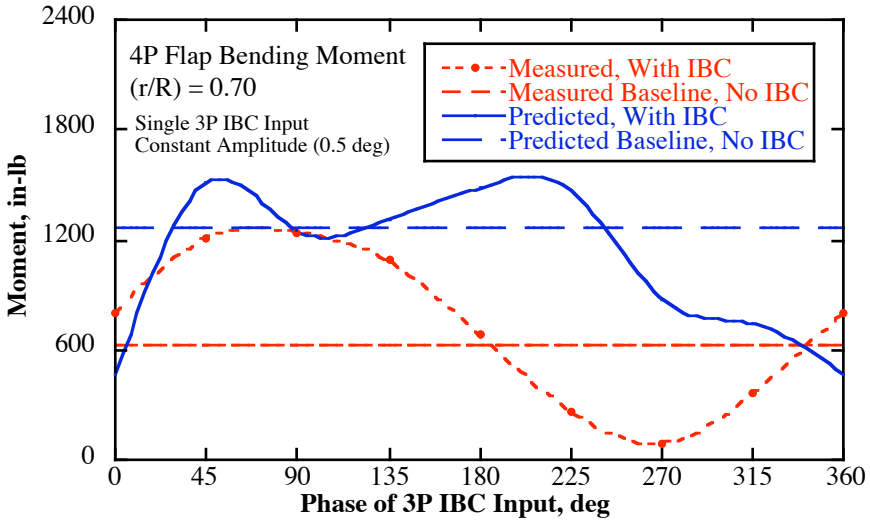

Fig. 32. Measured and predicted (CAMRAD II) UH-60A 4P flap bending moment variations with 3P IBC input phase, (r/R) = 0.70, $\mu = 0.107$, $C_T/\sigma = 0.0733$.